Zero-Backflow Power Control Scheme of Dual Bridge Series Resonant DC–DC Converters With High-Accuracy Time Domain Modeling

Yaru Deng, *Student Member, IEEE*, Wensheng Song, *Senior Member, IEEE*, Shuai Yin, Ming Zhong, Jian Chen, *Member, IEEE*, and Xiaoyun Feng

***Abstract*—In the fundamental harmonic approximation (FHA) modeling of dual bridge series resonant dc–dc converters (DBSRCs), the approximation error of the FHA model will lead to low accuracy of optimization schemes, which will reduce the efficiency of DBSRCs. In this article, first, the time domain analysis (TDA) modeling of the DBSRC is adopted, which can describe the characteristics of the DBSRC accurately. Second, the extended phase shift modulation based on the TDA modeling is discussed, and the backflow power model with the TDA of the DBSRC is developed. On this basis, a zero-backflow power optimization scheme is proposed. In addition, the effects of dead time are analyzed and the compensation method is proposed. The proposed backflow power optimization method with dead time compensation can achieve zero-backflow power and improve the efficiency of the DBSRC. Especially, the proposed method with TDA modeling is more excellent when DBSRC operates in wide voltage range conditions. Finally, a comprehensive experiment comparison of DBSRC under the minimum current trajectory with FHA modeling and the proposed method with TDA modeling is discussed. The experimental results have verified the effectiveness of the proposed scheme.**

***Index Terms*—Backflow power optimization, dead time compensation, dual bridge series resonant dc–dc converters (DBSRCs), time domain analysis (TDA) method.**

I. Introduction

THE bidirectional dc–dc converter is an important equipment for electric energy conversion, which can complete the power conversion between various levels of dc-bus [1], [2]. Dual bridge series resonant converters (DBSRCs) have the advantages of bidirectional power transmission, convenient switching of power flow, 3-high (high frequency, high efficiency, and high power density), and soft switching performance. Furthermore, with the development of optimization schemes of dc–dc converters and the availability of wide band-gap devices, such as SiC MOSFETs [3], dual active bridge dc–dc converters (DABCs) and DBSRCs are widely used as the interface between different dc-bus voltage levels. DABCs and DBSRCs have broad application prospects, such as energy storage systems [4], [5], [6], dc microgrid [7], [8], and middle-frequency railway traction systems [9], [10], as shown in Fig. 1. Besides, DBSRCs have become the critical equipment in uninterruptible power supplies and regenerative braking systems of electric rail and hybrid vehicles [11], [12], [13].

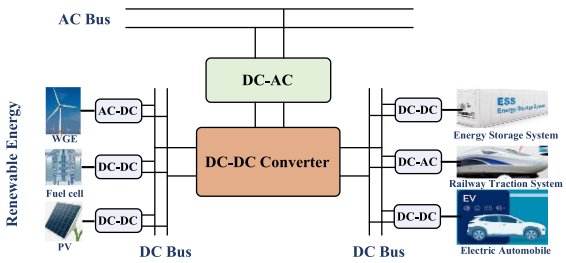

Fig. 1. Application of bidirectional DC–DC converters.

Phase-shift modulation is one of the classical control methods for bidirectional dc-dc converters. Single phase shift (SPS) modulation, may offer poor power efficiency, especially when the input voltage and output voltage are mismatched [14], [15]. Thus, advanced modulation methods, such as dual phase shift modulation [16], extended phase shift (EPS) modulation [17], and triple phase shift (TPS) modulation [18] are proposed to expand the ZVS range and improve the efficiency of DABCs.

DBSRCs have been proposed in [19], which combine some of the advantages of series resonant converters and DABCs. The resonant capacitor can eliminate the transient dc bias and the resonant process can reduce the switching loss of the DBSRC [20]. There have been many research works on modeling analysis methods, optimization strategies, and resonant parameter design schemes for the DBSRC. In general, the optimization strategies of the DBSRC are mainly proposed to improve the

Manuscript received 2 December 2022; revised 7 March 2023 and 27 April 2023; accepted 15 May 2023. Date of publication 24 May 2023; date of current version 28 July 2023. This work was supported in part by the Sichuan Youth Science and Technology Innovation Research Team under Grant 22CXTD0055, in part by the Sichuan Science and Technology Program under Grant 2023YFH0050, and in part by the National Natural Science Foundation of China under Grant U1934204. Recommended for publication by Associate Editor G. Moschopoulos. *(Corresponding authors: Wensheng Song; Xiaoyun Feng.)*

Yaru Deng, Wensheng Song, Shuai Yin, Jian Chen, and Xiaoyun Feng are with the School of Electrical Engineering, Southwest Jiaotong University, Chengdu 611756, China (e-mail: yaru_deng_swjtu@163.com; songwengsheng@163.com; ys2434984249@163.com; chenjian@swjtu.edu.cn; fengxy@home.swjtu.edu.cn).

Ming Zhong was with the School of Electrical Engineering, Southwest Jiaotong University, Chengdu 611756, China. He is now with the Huawei Technologies Company, Ltd., Chengdu 518129, China (e-mail: m_zhong_2018@163.com).

Color versions of one or more figures in this article are available at https://doi.org/10.1109/TPEL.2023.3279435.

Digital Object Identifier 10.1109/TPEL.2023.3279435

efficiency by reducing the root mean square value of resonant current, expanding the ZVS range, or reducing the backflow power.

The conventional SPS control cannot achieve high efficiency when the input and output voltages of the DBSRC are mismatched. Thus, a minimum current trajectory (MCT) method based on TPS control is proposed to reduce the conduction losses of the DBSRC [21]. But the efficiency under light load operation is still low, especially in the mismatch condition of the input and output voltages. A modified MCT, (M-MCT) method is proposed to improve the efficiency under light load operation [22]. However, MCT and M-MCT will lose ZVS under light load operation, and the efficiency of DBSRCs will reduce.

A four-degree-of-freedom control algorithm can realize ZVS and eliminate the backflow power, simultaneously [23]. But the circuit parameter optimization of the DBSRC is extremely complicated. When the parameters of the DBSRC are not selected properly, the system will generate large backflow power and reduce efficiency [24]. In addition, a backflow power minimization with the whole operating range for a modular multi-active-bridge converter is proposed in [25], and a zero-backflow power optimization based on TPS control is proposed in [26]. However, the above-all efficiency optimization methods of the DBSRC are based on the fundamental harmonic approximation (FHA) modeling. The FHA modeling is an approximate analysis method, which only has high accuracy near the resonant frequency point [27]. There is a discrepancy between the results obtained by the FHA model and the actual model. The discrepancy may cause some switches to lose ZVS [28] when the optimization methods are based on the FHA modeling, such as backflow power optimization. Thus, the efficiency optimization based on the FHA model of the DBSRC is not satisfactory.

To establish an accurate model of the DBSRC, extended harmonics approximation [29] considers higher harmonics to improve the modeling accuracy, but it increases the calculation amount. The state plane approach (SPA) [30] is used to obtain an accurate computational model. But the SPA method is very complicated in the calculation and derivation process. The frequency domain model of the DBSRC under SPS control is established in [31]. However, the mathematical expression of the resonant current is complex and difficult to solve and optimize. Small-signal modeling under SPS control can obtain the transfer function of the DBSRC [32]. But a small-signal model of DBSRC under multiphase shift control [33] is too complicated to be applied in practice. A relatively accurate output voltage model of DBSRC is established by the extended description function method [34], which can analyze the output dynamic characteristics of DBSRC as much as possible.

Besides, the time domain analysis (TDA) method is an accurate modeling method, which can accurately analyze the DBSRC. In [35], under the SPS control, the instantaneous expressions of the resonant tank current and transmission power of DBSRC are calculated by the TDA method, which can overcome the disadvantage of the FHA method. A global optical method based on the TDA model under EPS modulation has been proposed in [36]. However, it is complex to implement and harder to optimize the magnetics and filter because both phase shift control and variable frequency control are used. Besides, there are few reports about the TDA modeling of DBSRCs, systematically. It is significant to explore multiphase shift control and other optical methods based on the TDA method.

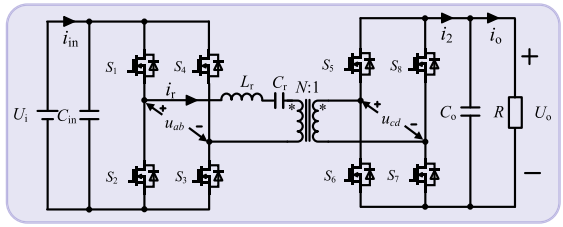

Fig. 2. Topology of the DBSRC.

In this article, an accurate mathematical model of the DBSRC under EPS modulation is analyzed based on the TDA modeling. In Section II, four operating modes of the DBSRC under EPS modulation are discussed. Besides, the transmission power of the DBSRC under EPS based on the TDA method is analyzed. In Section III, the backflow power models in four modes of the DBSRC are analyzed, respectively. On this basis, the realization boundary of zero-backflow power is analyzed. A zero-backflow power control scheme under EPS of the DBSRC based on TDA modeling is proposed in Section IV. In addition, the dead time effects are analyzed and the compensation method is proposed. In Section V, an experimental prototype of the DBSRC is developed, and a comprehensive experiment comparison between the MCT with FHA modeling and the proposed method with TDA modeling is discussed in detail. Section VI concludes this article.

II. Fundamental and Time Domain Modeling for DBSRC

A. Fundamental of DBSRC Under EPS Modulation

As shown in Fig. 2, the topology of the DBSRC mainly consists of two symmetrical full H-bridges, a high-frequency isolation transformer, and a series resonant tank. $U_{\rm i}$ is the input voltage and $U_{\rm o}$ is the output voltage. $u_{\rm ab}$ and $u_{\rm cd}$ are the voltages at the input and output terminals of the transformer, respectively. N is the transformer voltage ratio. $L_{\rm r}$ and $C_{\rm r}$ represent the resonant inductor and capacitor of the series resonant tank, respectively. $i_{\rm r}$ is the resonant current, and $i_{\rm in}$ is the input current. $C_{\rm i}$ and $C_{\rm o}$ represent the input and output capacitors, respectively. i_2 is the output current of the secondary-side H-bridge, and $i_{\rm o}$ represents the load current.

Phase shift modulation is one of the classical control methods of the DBSRC. The degree of optimization and functional diversity of the DBSRC is positively related to the number of controllable phase shift variables. Combined with the characteristics of phase shift modulation, EPS modulation is chosen to achieve backflow power optimization and efficiency improvement of the DBSRC in this article. The switching pulse, square wave voltage $u_{\rm ab}$ and $u_{\rm cd}$, and resonant current $i_{\rm r}$ are shown in Fig. 3. θ represents the outer phase shift, φ_1 $(0 < \varphi_1 < \pi)$ is the inner phase shift of the primary H-bridge, and φ_2 $(0 < \varphi_2 < \pi)$ is

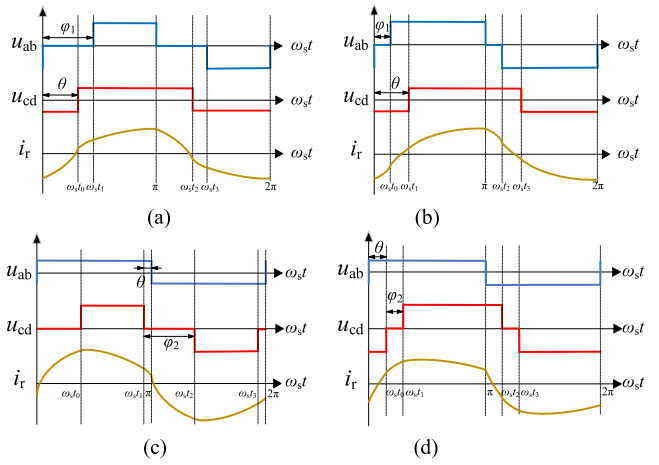

Fig. 3. Waveforms of the DBSRC under EPS control. (a) Mode I. (b) Mode II. (c) Mode III. and (d) Mode IV.

TABLE I
RESONANT TANK VOLTAGE

Modes	Stage A	Stage B	Stage C
I	NU_o	-NU_o	U_i-NU_o
II	NU_o	U_i+NU_o	U_i-NU_o
III	U_i	U_i-NU_o	U_i
IV	U_i+NU_o	U_i	U_i-NU_o

the inner phase shift of secondary H-bridge. ω_s is the switching angular frequency, $\omega_s = 2\pi f_s$, and f_s is the switching frequency. When the output power is constant, φ_1 or φ_2 can be controlled to make the backflow power decrease and the efficiency increase of the DBSRC. When the resonant current crosses the zero point ($0 \le \omega_s t \le \pi$), the phase shift is $\omega_s t = \alpha$, which means that $i_r(\alpha) = 0$. The voltage conversion ratio is $K = NU_o / U_i$. In EPS modulation, the four operating modes of the DBSRC are shown in Fig. 3(a)–(d). When $K \le 1$ the operating modes of DBSRC are Mode I and Mode II. When $K > 1$, the operating modes of DBSRC are Mode III and Mode IV.

B. TDA Model of DBSRC Under EPS Modulation

Compared with the FHA model, the precise TDA model provides the opportunity for the optimization control scheme to improve the efficiency and control accuracy of the DBSRC. When $0 \le \omega_s t \le \pi$, there are three stages of resonant tank voltage u_r. Take Mode I as an example, the three stages are defined as Stage A: when $0 \le \omega_s t \le \omega_s t_0$, $u_r = NU_o$, Stage B: when $\omega_s t_0 \le \omega_s t \le \omega_s t_1$, $u_r =$ - NU_o, and Stage C: when $\omega_s t_1 \le \omega_s t \le \pi$, $u_r = U_i$ - NU_o. The expressions of Mode II, Mode III, and Mode IV of the resonant voltage u_r during Stage A-C are shown in Table I.

The resonator characteristic impedance Z_r and frequency ratio F are defined as

$$Z_r = \sqrt{L_r/C_r}, f_r = 1\Big/\left(2\pi\sqrt{L_r C_r}\right), \quad F = f_s/f_r \tag{1}$$

where f_r is the resonant frequency, and $F > 1$.

Due to the symmetry of the DBSRC, the working processes of the first half switching period and the second half switching period of the DBSRC are similar, which means

$$i_{Lr}(0) = -i_{Lr}(\pi),\ u_{Cr}(0) = -u_{Cr}(\pi) \tag{2}$$

where u_{Cr} is the resonant capacitor voltage, i_{Lr} is the resonant inductor current, which is the resonant tank current i_r, too.

Thus, the resonant tank voltage can be expressed as

$$u_r = u_{Cr} + L_r \frac{di_{Lr}}{dt} = u_{Cr} + L_r C_r \frac{d^2 u_{Cr}}{dt^2}. \tag{3}$$

The resonant tank voltage and current can be solved by (3)

$$i_r(\omega_s t) = i_r(\omega_s t_x)\cos\left(\frac{\omega_s t - \omega_s t_x}{F}\right) + \left[\frac{u_r - u_{C_r}(\omega_s t_x)}{Z_r}\right]\sin\left(\frac{\omega_s t - \omega_s t_x}{F}\right),\ t \in [t_x, t_y] \tag{4}$$

$$u_{C_r}(\omega_s t) = i_r(\omega_s t_x) Z_r \sin\left(\frac{\omega_s t - \omega_s t_x}{F}\right) + u_r - [u_r - u_{C_r}(\omega_s t_x)]\cos\left(\frac{\omega_s t - \omega_s t_x}{F}\right),\ t \in [t_x, t_y] \tag{5}$$

where $[t_x, t_y] = [0, t_0]$ in Stage A, $[t_x, t_y] = [t_0, t_1]$ in Stage B, and $[t_x, t_y] = [t_1, \pi/\omega_s]$ in Stage C.

When the DBSRC works in Mode I, the differential equations of resonant tank current and voltage are established on Stage A-C, respectively. Based on (2), the matrix expression can be obtained, which is shown in (6) shown at the bottom of the next page. Where the matrix $\boldsymbol{G}$ is related to the phase shift variables, the matrix $\boldsymbol{F}$ is related to the working mode and the input and output voltages of the converter. Matrix $\boldsymbol{x}$ is the initial value of the resonant tank current and the resonant capacitance voltage at each stage, which is determined by the matrices $\boldsymbol{G}$ and $\boldsymbol{F}$. The matrix $\boldsymbol{x}$ can be obtained by solving (6), and the initial values of the resonant inductance current and resonant capacitance voltage at each stage are shown in Appendices I. Then, the expression of the resonant tank current at Stage A-C can be obtained as shown in (7) shown at the bottom of the next page. Besides, the process of analysis in the second half cycle is similar to that in the first half cycle, so it is not analyzed.

According to the assumption, ignoring the losses of the converter, the transmission power can be expressed as (8) shown at the bottom of the next page. The analysis processes of Mode II-IV are similar to those of Mode I, and the resonant tank current expressions of Mode II-IV under EPS control can be obtained as shown in (9)–(11) shown at the bottom of the next page, respectively. The initial values of Mode II-IV are shown in Appendices I, too. Besides, according to the resonant tank current expressions of Modes II, III, and IV, the transmission power of the converter can be obtained as (12) shown at the bottom of the next page.

III. BACKFLOW POWER MODEL AND OPTIMIZATION STRATEGY

A. Backflow Power Model of DBSRC

Based on the TDA model of the DBSRC, Q_1 and Q_2 are the backflow powers of the primary and secondary side of the converter, respectively. In Mode I: it is shown in Fig. 3(a)

that there is no backflow power on the primary side. And the expressions of the backflow power of the primary and secondary sides can be obtained as

$$\begin{cases} Q_1 = 0 \\ Q_2 = \frac{1}{\pi}\left|\int_{\alpha}^{\theta} u_{\mathrm{cd}} i_{\mathrm{r}} d(\omega_{\mathrm{s}} t)\right| \end{cases}. \tag{13}$$

In Mode II: as shown in Fig. 3(b), the expressions of the backflow power of the primary and the secondary side are

$$\begin{cases} Q_1 = \frac{1}{\pi}\left|\int_{\varphi_1}^{\alpha} u_{\mathrm{ab}} i_{\mathrm{r}} d(\omega_{\mathrm{s}} t)\right| \\ Q_2 = \frac{1}{\pi}\left|\int_{\alpha}^{\theta} u_{\mathrm{cd}} i_{\mathrm{r}} d(\omega_{\mathrm{s}} t)\right| \end{cases}. \tag{14}$$

In Mode III: it is shown in Fig. 3(c) that there is no backflow power on the secondary side. And the expressions of the backflow power of the primary and secondary sides can be obtained as

$$\begin{cases} Q_1 = \frac{1}{\pi}\left|\int_{0}^{\alpha} u_{\mathrm{ab}} i_{\mathrm{r}} d(\omega_{\mathrm{s}} t)\right| \\ Q_2 = 0 \end{cases}. \tag{15}$$

In Mode IV: as shown in Fig. 3(d), there is backflow power in both the primary and secondary sides, the expressions are

$$\begin{cases} Q_1 = \frac{1}{\pi}\left|\int_{0}^{\alpha} u_{\mathrm{ab}} i_{\mathrm{r}} d(\omega_{\mathrm{s}} t)\right| \\ Q_2 = \frac{1}{\pi}\left|\int_{\alpha}^{\theta} u_{\mathrm{cd}} i_{\mathrm{r}} d(\omega_{\mathrm{s}} t)\right| \end{cases}. \tag{16}$$

Equations (13)–(16) can be calculated as (17)–(20) shwon at the bottom of the next page, which are the expressions of the backflow power in Modes I–IV

$$\boldsymbol{Gx} = \boldsymbol{F} \rightarrow \begin{bmatrix} \cos(\frac{\theta}{F}) & -\sin(\frac{\theta}{F}) & -1 & 0 & 0 & 0 \\ \sin(\frac{\theta}{F}) & \cos(\frac{\theta}{F}) & 0 & -1 & 0 & 0 \\ 0 & 0 & \cos(\frac{\varphi_1-\theta}{F}) & -\sin(\frac{\varphi_1-\theta}{F}) & -1 & 0 \\ 0 & 0 & \sin(\frac{\varphi_1-\theta}{F}) & \cos(\frac{\varphi_1-\theta}{F}) & 0 & -1 \\ -1 & 0 & 0 & 0 & \cos(\frac{\pi-\varphi_1}{F}) & -\sin(\frac{\pi-\varphi_1}{F}) \\ 0 & -1 & 0 & 0 & \sin(\frac{\pi-\varphi_1}{F}) & \cos(\frac{\pi-\varphi_1}{F}) \end{bmatrix} \begin{bmatrix} Z_{\mathrm{r}} i_{\mathrm{r}}(0) \\ u_{\mathrm{C_r}}(0) \\ Z_{\mathrm{r}} i_{\mathrm{r}}(\theta) \\ u_{\mathrm{C_r}}(\theta) \\ Z_{\mathrm{r}} i_{\mathrm{r}}(\varphi_1) \\ u_{\mathrm{C_r}}(\varphi_1) \end{bmatrix}$$

$$= -\begin{bmatrix} \sin(\frac{\theta}{F})(NU_{\mathrm{o}}) \\ [1-\cos(\frac{\theta}{F})](NU_{\mathrm{o}}) \\ \sin(\frac{\varphi_1-\theta}{F})(-NU_{\mathrm{o}}) \\ [1-\cos(\frac{\varphi_1-\theta}{F})](-NU_{\mathrm{o}}) \\ \sin(\frac{\pi-\varphi_1}{F})(U_{\mathrm{i}}-NU_{\mathrm{o}}) \\ [1-\cos(\frac{\pi-\varphi_1}{F})](U_{\mathrm{i}}-NU_{\mathrm{o}}) \end{bmatrix} \tag{6}$$

$$\text{Mode I}: i_{\mathrm{r}}(\omega_{\mathrm{s}} t) = \begin{cases} i_{\mathrm{r}}(0)\cos(\frac{\omega_{\mathrm{s}} t}{F}) + \frac{[NU_{\mathrm{o}}-u_{\mathrm{C_r}}(0)]}{Z_{\mathrm{r}}}\sin(\frac{\omega_{\mathrm{s}} t}{F}) & \omega_{\mathrm{s}} t \in [0,\theta] \\ i_{\mathrm{r}}(\theta)\cos(\frac{\omega_{\mathrm{s}} t-\theta}{F}) + \frac{[-NU_{\mathrm{o}}-u_{\mathrm{C_r}}(\theta)]}{Z_{\mathrm{r}}}\sin(\frac{\omega_{\mathrm{s}} t-\theta}{F}) & \omega_{\mathrm{s}} t \in [\theta,\varphi_1] \\ i_{\mathrm{r}}(\varphi_1)\cos(\frac{\omega_{\mathrm{s}} t-\varphi_1}{F}) + \frac{[U_{\mathrm{i}}-NU_{\mathrm{o}}-u_{\mathrm{C_r}}(\varphi_1)]}{Z_{\mathrm{r}}}\sin(\frac{\omega_{\mathrm{s}} t-\varphi_1}{F}) & \omega_{\mathrm{s}} t \in [\varphi_1,\pi] \end{cases} \tag{7}$$

$$P_{\mathrm{o}} = U_{\mathrm{o}} I_{\mathrm{o}} = \frac{1}{2\pi}\int_0^{2\pi} u_{\mathrm{ab}} i_{\mathrm{r}} d(\omega_{\mathrm{s}} t) = \frac{2NU_{\mathrm{i}}U_{\mathrm{o}}}{\pi Z_{\mathrm{r}}} F \sec\left(\frac{\pi}{2F}\right)\sin\left(\frac{2\theta-\varphi_1}{2F}\right)\sin\left(\frac{\pi-\varphi_1}{2F}\right) \tag{8}$$

$$\text{Mode II}: i_{\mathrm{r}}(\omega_{\mathrm{s}} t) = \begin{cases} i_{\mathrm{r}}(0)\cos(\frac{\omega_{\mathrm{s}} t}{F}) + \frac{[NU_{\mathrm{o}}-u_{\mathrm{C_r}}(0)]}{Z_{\mathrm{r}}}\sin(\frac{\omega_{\mathrm{s}} t}{F}) & \omega_{\mathrm{s}} t \in [0,\varphi_1] \\ i_{\mathrm{r}}(\varphi_1)\cos(\frac{\omega_{\mathrm{s}} t-\varphi_1}{F}) + \frac{[U_{\mathrm{i}}+NU_{\mathrm{o}}-u_{\mathrm{C_r}}(\varphi_1)]}{Z_{\mathrm{r}}}\sin(\frac{\omega_{\mathrm{s}} t-\varphi_1}{F}) & \omega_{\mathrm{s}} t \in [\varphi_1,\theta] \\ i_{\mathrm{r}}(\theta)\cos(\frac{\omega_{\mathrm{s}} t-\theta}{F}) + \frac{[U_{\mathrm{i}}-NU_{\mathrm{o}}-u_{\mathrm{C_r}}(\theta)]}{Z_{\mathrm{r}}}\sin(\frac{\omega_{\mathrm{s}} t-\theta}{F}) & \omega_{\mathrm{s}} t \in [\theta,\pi] \end{cases} \tag{9}$$

$$\text{Mode III}: i_{\mathrm{r}}(\omega_{\mathrm{s}} t) = \begin{cases} i_{\mathrm{r}}(0)\cos(\frac{\omega_{\mathrm{s}} t}{F}) + \frac{[U_{\mathrm{i}}-u_{\mathrm{C_r}}(0)]}{Z_{\mathrm{r}}}\sin(\frac{\omega_{\mathrm{s}} t}{F}) & \omega_{\mathrm{s}} t \in [0,\varphi_2-\theta] \\ i_{\mathrm{r}}(\varphi_2-\theta)\cos(\frac{\omega_{\mathrm{s}} t-\varphi_2+\theta}{F}) + \frac{[U_{\mathrm{i}}-NU_{\mathrm{o}}-u_{\mathrm{C_r}}(\varphi_2-\theta)]}{Z_{\mathrm{r}}}\sin(\frac{\omega_{\mathrm{s}} t-\varphi_2+\theta}{F}) & \omega_{\mathrm{s}} t \in [\varphi_2-\theta,\pi-\theta] \\ i_{\mathrm{r}}(\pi-\theta)\cos(\frac{\omega_{\mathrm{s}} t-\pi+\theta}{F}) + \frac{[U_{\mathrm{i}}-u_{\mathrm{C_r}}(\pi-\theta)]}{Z_{\mathrm{r}}}\sin(\frac{\omega_{\mathrm{s}} t-\pi+\theta}{F}) & \omega_{\mathrm{s}} t \in [\pi-\theta,\pi] \end{cases} \tag{10}$$

$$\text{Mode IV}: i_{\mathrm{r}}(\omega_{\mathrm{s}} t) = \begin{cases} i_{\mathrm{r}}(0)\cos(\frac{\omega_{\mathrm{s}} t}{F}) + \frac{[U_{\mathrm{i}}+NU_{\mathrm{o}}-u_{\mathrm{C_r}}(0)]}{Z_{\mathrm{r}}}\sin(\frac{\omega_{\mathrm{s}} t}{F}) & \omega_{\mathrm{s}} t \in [0,\theta] \\ i_{\mathrm{r}}(\theta)\cos(\frac{\omega_{\mathrm{s}} t-\theta}{F}) + \frac{[U_{\mathrm{i}}-u_{\mathrm{C_r}}(\theta)]}{Z_{\mathrm{r}}}\sin(\frac{\omega_{\mathrm{s}} t-\theta}{F}) & \omega_{\mathrm{s}} t \in [\theta,\theta+\varphi_2] \\ i_{\mathrm{r}}(\theta+\varphi_2)\cos(\frac{\omega_{\mathrm{s}} t-\theta-\varphi_2}{F}) + \frac{[U_{\mathrm{i}}-NU_{\mathrm{oi}}-u_{\mathrm{C_r}}(\theta+\varphi_2)]}{Z_{\mathrm{r}}}\sin(\frac{\omega_{\mathrm{s}} t-\theta-\varphi_2}{F}) & \omega_{\mathrm{s}} t \in [\theta+\varphi_2,\pi] \end{cases}. \tag{11}$$

$$P_{\mathrm{o}} = \begin{cases} \frac{2NU_{\mathrm{i}}U_{\mathrm{o}}}{\pi Z_{\mathrm{r}}} F \sec\left(\frac{\pi}{2F}\right)\sin\left(\frac{2\theta-\varphi_1}{2F}\right)\sin\left(\frac{\pi-\varphi_1}{2F}\right) & \text{Mode I} \\ \frac{2NU_{\mathrm{i}}U_{\mathrm{o}}}{\pi Z_{\mathrm{r}}} F \sec\left(\frac{\pi}{2F}\right)\left[\cos\left(\frac{\varphi_1}{2F}\right)\cos\left(\frac{\pi-2\theta+\varphi_1}{2F}\right)-\cos\left(\frac{\pi}{2F}\right)\right] & \text{Mode II} \\ \frac{2NU_{\mathrm{i}}U_{\mathrm{o}}}{\pi Z_{\mathrm{r}}} F \sec\left(\frac{\pi}{2F}\right)\sin\left(\frac{\varphi_2}{2F}\right)\sin\left(\frac{\varphi_2-2\theta}{2F}\right) & \text{Mode III} \\ \frac{2NU_{\mathrm{i}}U_{\mathrm{o}}}{\pi Z_{\mathrm{r}}} F \sec\left(\frac{\pi}{2F}\right)\left[\cos\left(\frac{\varphi_2}{2F}\right)\cos\left(\frac{\pi-2\theta-\varphi_2}{2F}\right)-\cos\left(\frac{\pi}{2F}\right)\right] & \text{Mode IV} \end{cases}. \tag{12}$$

B. Zero-Backflow Power Optimization Strategy

Based on the analysis of the backflow power model, the backflow power will increase the on-sate loss and reduce the efficiency of the DBSRC. Besides, the expressions of the backflow power are complicated to solve. According to the principle, the resonant tank current can be controlled by regulating the phase shift, and the backflow power can be optimized.

When $K \leq 1$, the operation mode of the DBSRC is Mode III and Mode IV, which is shown in Fig. 3(a) and (b), respectively. The backflow power under EPS modulation can be optimized by adjusting the inner phase shift φ_1. The resonant tank current meets the limitation of the zero-backflow power of the secondary side Q_2, which means that $Q_2 = 0$. The limitation of the zero-backflow power of the secondary side is

$$i_{\mathrm{r}}(\theta) = 0 \tag{21}$$

when $K > 1$, the operation mode of the DBSRC is Mode III and Mode IV, which is shown in Fig. 3(c) and (d), respectively. The limitation of the zero-backflow power of the primary side is

$$i_{\mathrm{r}}(0) = 0. \tag{22}$$

According to the principle of backflow power optimization, as long as the output voltage of the H-bridge is zero during the power backflow period, the power backflow is zero. The switching period in which the H-bridge output voltage phase is opposite to the resonant tank current phase can be decreased by controlling φ_1 or φ_2 of the EPS method. Then the backflow power can be reduced and the efficiency can be increased.

IV. Accurate Zero-Backflow Power Optimization

A. Analysis of the Proposed Method

An accurate TDA with EPS modulation method is proposed to realize zero-backflow power optimization, which can further improve the efficiency of the DBSRC. As shown in Fig. 4(a), if the resonant tank current crosses zero at the outer phase shift θ, the zero-backflow power can be achieved in Mode I. According to (21), to realize the backflow power optimization of the DBSRC, the optimal results can be obtained with the expression of the resonant tank current.

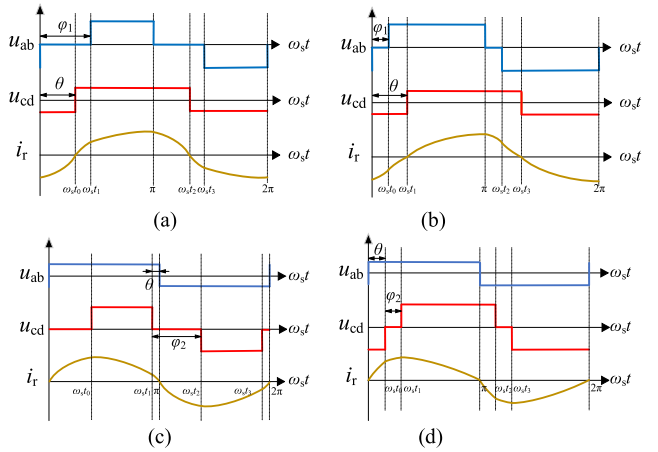

Fig. 4. Schematic diagram of zero-backflow power optimization method. (a) Mode I. (b) Mode II. (c) Mode III. and (d) Mode IV.

Take Mode I as an example, according to (7), $i_{\mathrm{r}}(\theta) = 0$ can be expressed as

$$U_{\mathrm{i}}\left[\sin\left(\frac{\theta}{F}\right) - \sin\left(\frac{\pi+\theta-\varphi_1}{F}\right) - \sin\left(\frac{\pi-\theta}{F}\right) + \sin\left(\frac{\varphi_1-\theta}{F}\right)\right] + 2NU_{\mathrm{o}}\sin\left(\frac{\pi}{F}\right) = 0. \tag{23}$$

Mode I

$$\begin{cases} Q_1 = 0 \\ Q_2 = \frac{NU_{\mathrm{i}}U_{\mathrm{o}}}{\pi^2 Z_{\mathrm{r}}} F \sec\left(\frac{\pi}{2F}\right) \left[\begin{array}{l} \sqrt{\sin^2\left(\frac{\varphi_1-\pi}{2F}\right) + K^2 + 2K\sin\left(\frac{\varphi_1}{2F}\right)\sin\left(\frac{\varphi_1-2\theta+2\pi}{2F}\right)} \\ -\sin\left(\frac{\varphi_1-2\pi}{2F}\right)\sin\left(\frac{\varphi_1-2\phi}{2F}\right) - K\cos\left(\frac{\pi}{2F}\right) \end{array}\right] \end{cases} \tag{17}$$

Mode II

$$\begin{cases} Q_1 = \frac{NU_{\mathrm{i}}U_{\mathrm{o}}}{\pi^2 K Z_{\mathrm{r}}} F \sec\left(\frac{\pi}{2F}\right) \left[\begin{array}{l} \cos\left(\frac{\varphi_1}{2F}\right)\cos\left(\frac{\pi-\varphi_1}{2F}\right) + K\cos\left(\frac{\pi-2\theta+2\varphi_1}{2F}\right) \\ -\sqrt{\sec\left(\frac{\pi}{2F}\right)\cos\left(\frac{\varphi_1}{2F}\right)\cos\left(\frac{\pi-\varphi_1}{2F}\right) + K^2 + 2K\cos\left(\frac{\varphi_1}{2F}\right)\cos\left(\frac{2\pi-2\theta+\varphi_1}{2F}\right)} \end{array}\right] \\ Q_2 = \frac{NU_{\mathrm{i}}U_{\mathrm{o}}}{\pi^2 Z_{\mathrm{r}}} F \sec\left(\frac{\pi}{2F}\right) \left[\begin{array}{l} \sqrt{\sec\left(\frac{\pi}{2F}\right)\cos\left(\frac{\varphi_1}{2F}\right)\cos\left(\frac{\pi-\varphi_1}{2F}\right) + K^2 + 2K\cos\left(\frac{\varphi_1}{2F}\right)\cos\left(\frac{2\pi-2\theta+\varphi_1}{2F}\right)} \\ -\cos\left(\frac{\varphi_1}{2F}\right)\cos\left(\frac{\pi-2\theta+\varphi_1}{2F}\right) - K\cos\left(\frac{\pi}{2F}\right) \end{array}\right] \end{cases} \tag{18}$$

Mode III

$$\begin{cases} Q_1 = \frac{NU_{\mathrm{i}}U_{\mathrm{o}}}{\pi^2 K Z_{\mathrm{r}}} F \sec\left(\frac{\pi}{2F}\right) \left[\begin{array}{l} \cos\left(\frac{\pi}{2F}\right) - K\sin\left(\frac{\varphi_2-2\theta}{2F}\right)\sin\left(\frac{\varphi_2-\pi}{2F}\right) \\ -\sqrt{1 + K^2\sin^2\left(\frac{\pi-\varphi_2}{2F}\right) + K\left[\cos\left(\frac{\pi-\theta}{F}\right) - \cos\left(\frac{\varphi_2-\theta}{F}\right)\right]} \end{array}\right] \\ Q_2 = 0 \end{cases} \tag{19}$$

Mode IV

$$\begin{cases} Q_1 = \frac{NU_{\mathrm{i}}U_{\mathrm{o}}}{\pi^2 K Z_{\mathrm{r}}} F \sec\left(\frac{\pi}{2F}\right) \left[\begin{array}{l} \cos\left(\frac{\pi}{2F}\right) + K\cos\left(\frac{\varphi_2}{2F}\right)\cos\left(\frac{\pi-2\theta-\varphi_2}{2F}\right) \\ -\sqrt{1 + K^2\cos^2\left(\frac{\varphi_2}{2F}\right) + 2K\cos\left(\frac{\varphi_2}{2F}\right)\cos\left(\frac{\varphi_2+2\theta-2\pi}{2F}\right)} \end{array}\right] \\ Q_2 = \frac{NU_{\mathrm{i}}U_{\mathrm{o}}}{\pi^2 Z_{\mathrm{r}}} F \sec\left(\frac{\pi}{2F}\right) \left[\begin{array}{l} \sqrt{1 + K^2\cos^2\left(\frac{\varphi_2}{2F}\right) + 2K\cos\left(\frac{\varphi_2}{2F}\right)\cos\left(\frac{\varphi_2+2\theta-2\pi}{2F}\right)} \\ -\cos\left(\frac{\pi-2\theta}{2F}\right) - K\cos\left(\frac{\varphi_2}{2F}\right)\cos\left(\frac{\varphi_2-\pi}{2F}\right) \end{array}\right] \end{cases}. \tag{20}$$

To simplify (23), the relationship between the outer phase shift θ and the inner phase shift φ_1 can be obtained as

$$\text{Mode I}: \ \varphi_1 = \theta + \frac{\pi}{2} - Far\sin(T_1) \tag{24}$$

$$T_1 = \sin\left(\frac{2\theta-\pi}{2F}\right) + 2K\sin\left(\frac{\pi}{2F}\right). \tag{25}$$

Similarly, in Mode II, the resonant tank current should satisfy the limitations of the zero-backflow power of the secondary side, shown in (21). The optimal results can be obtained with the expression of the resonant tank current of Mode II, which is expressed as

$$U_{\rm i}\left[\sin\left(\frac{\pi-\theta}{F}\right) + \sin\left(\frac{\pi-\theta+\varphi_1}{F}\right) - \sin\left(\frac{\theta-\varphi_1}{F}\right) - \sin\left(\frac{\theta}{F}\right)\right] - 2NU_{\rm o}\sin\left(\frac{\pi}{F}\right) = 0. \tag{26}$$

To simplify (26), the relationship between the outer phase shift θ and the inner phase shift φ_1 can be obtained as

$$\text{Mode II}: \varphi_1 = \theta - \frac{\pi}{2} + Far\sin(T_1). \tag{27}$$

The schematic diagram in Mode II of the proposed method with TDA modeling is shown in Fig. 4(b). When $K \le 1$, the zero-backflow power of the secondary side can be achieved with the limitation in (21).

Approximatively, when $K > 1$, based on the limitation of (22), the analysis process of Mode III and Mode IV is ignored and the optimal results are expressed as

$$\begin{cases} \text{Mode III}: \varphi_2 = \frac{\pi}{2} + \theta - Far\sin(T_2) \\ \text{Mode IV}: \varphi_2 = \frac{\pi}{2} - \theta - Far\sin(T_2) \end{cases} \tag{28}$$

$$T_2 = \sin\left(\frac{2\theta-\pi}{2F}\right) + \frac{2}{K}\sin\left(\frac{\pi}{2F}\right). \tag{29}$$

The schematic diagram in Mode III and Mode IV of the proposed method with TDA modeling is shown in Fig. 4(c) and (d), respectively. Based on the analysis of the zero-backflow power optimization with the TDA model, the expressions of optimal inner phase shift are obtained as (30) shown at the bottom of this page,

$P_{\rm opu}$ is the per unit value of $P_{\rm o}$, $P_{\rm opu} = P_{\rm o}\pi Z_{\rm r} \,/\, 2NU_{\rm i}U_{\rm o}$. Based on the above analysis, the working principle of the DBSRC when $K > 1$ is similar to the working principle when $K \le 1$, thus, the theoretical and experimental analysis when $K > 1$ will not be repeated in the following sections.

B. Compensation Strategy for Dead Time Effects

DBSRCs are widely used in high-frequency applications, and the effects of dead time become more and more negligible when the switching frequency increases. The waveforms of the drive signals and the voltages of the anti-parallel diodes are shown in Fig. 5. As shown in Fig. 5(a), taking the bridge arm of S_1 and S_2 as an example, the effects of dead time when the switches achieve or lose ZVS are analyzed as follows.

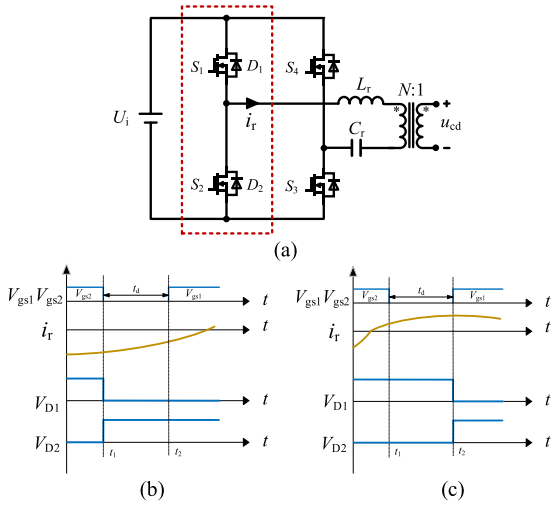

Fig. 5. The Effects of dead time when switches achieve or lose ZVS. (a) Topology of primary H-bridge of DBSRC. (b) Achieve ZVS. (c) Lose ZVS.

D_1 and D_2 are the antiparallel diodes of switches S_1 and S_2, respectively. $V_{\rm D1}$ and $V_{\rm D2}$ are the voltages of diodes D_1 and D_2. $V_{\rm gs1}$ and $V_{\rm gs2}$ are the drive signals of switches S_1 and S_2. $t_{\rm d}$ is the dead time. As shown in Fig. 5(b), S_2 off at t_1, $i_{\rm r}$ $(t_1) < 0$, D_1 on and $V_{\rm D1} = 0$. Thus, the S_1 achieves ZVS and the voltages $V_{\rm D1}$ and $V_{\rm D2}$ are not affected by dead time. However, when $i_{\rm r}$ $(t_1) > 0$ and S_2 off at t_1, which is shown in Fig. 5(c). D_2 on and $V_{\rm D1} \neq 0$. Until S_1 on at t_2, $V_{\rm D1} = 0$. The S_1 loses ZVS and the voltages $V_{\rm D1}$ and $V_{\rm D2}$ are affected by dead time. In summary, when switch S_1 achieves or loses ZVS, the diode voltage $V_{\rm D1}$ changes at the leading or trailing edges of the dead zone. The same is true for other switches. When the switches lose ZVS, there are deviations in the phase shift of the DBSRC caused by dead time, which is the phase drift phenomenon.

The limitation expressions of the zero-backflow power are derived ideally. The effects of dead time on the operation performance of the DBSRC are analyzed, and a compensation method is proposed to compensate for the error caused by dead time. The waveforms with dead time compensation of the DBSRC are shown in Fig. 6, which is under the proposed backflow power optimization method when $K \le 1$. Because only switches S_3 and S_4 in Mode I cannot realize ZVS, the dead time of switches S_3 and S_4 will lead to the phase drift phenomenon. However, all switches in Mode II can realize ZVS and the dead time does not affect phase shift. Thus, the phase drift phenomenon is analyzed in Mode I.

$$\begin{cases} \text{Mode I}: \varphi_1 = \theta + \frac{\pi}{2} - Far\sin(T_1), \ P_{\rm opu} \le \sqrt{1+(4K-4K^2)\tan^2(\pi/2F)} - 1 \\ \text{Mode II}: \varphi_1 = -\frac{\pi}{2} + Far\sin(T_1), \ P_{\rm opu} > \sqrt{1+(4K-4K^2)\tan^2(\pi/2F)} - 1 \\ \text{Mode III}: \varphi_2 = \frac{\pi}{2} + \theta - Far\sin(T_2), \ P_{\rm opu} \le \sqrt{1+(4/K-4/K^2)\tan^2(\pi/2F)} - 1 \\ \text{Mode IV}: \varphi_2 = \frac{\pi}{2} - \theta - Far\sin(T_2), \ P_{\rm opu} > \sqrt{1+(4/K-4/K^2)\tan^2(\pi/2F)} - 1 \end{cases} \tag{30}$$

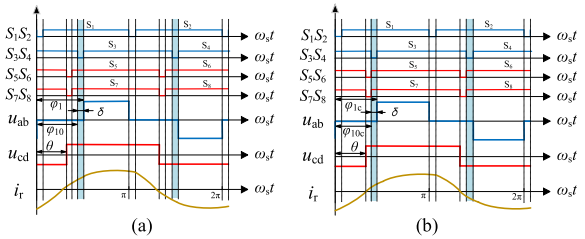

Fig. 6. Dead time compensation in mode I($K \leq 1$). (a) Without compensation. (b) With compensation.

As shown in Fig. 6(a), θ is the phase shift between the primary and the secondary side H-bridge. δ is the phase shift of dead time, $\delta = 2\pi f_s t_d$. The phase shift φ_1 and φ_{10} is the actual and theoretical phase shift without dead time compensation between the drive signals of switches S_1 and S_3, respectively. The relationship between φ_{10} and φ_1 can be expressed as

$$\varphi_1 = \varphi_{10} + \delta \tag{31}$$

where φ_{10} can be derived from (24) and (25). Because of the dead time effects, the phase shift φ_{10} maybe drift to φ_1. According to (20), to achieve the zero-backflow power optimization, the resonant current should be $i_r(\theta) = 0$, but because of dead time effects, the proposed method with TDA modeling cannot accurately achieve zero-backflow power optimization, as shown in Fig. 6(a). The influence of dead time increases with frequency increasing.

To eliminate the effects of dead time, a compensation method is proposed in Fig. 6(b). The inner phase shift φ_{10c} is the theoretical phase shift with dead time compensation between the drive signals of switches S_1 and S_3, which can be expressed as

$$\varphi_{10c} = \varphi_{10} - \delta. \tag{32}$$

Then, because of the phase drift phenomenon, the actual phase shift φ_{1c} with dead time compensation between the drive signals of switches S_1 and S_3 is

$$\varphi_{1c} = \varphi_{10c} + \delta = \varphi_{10} - \delta + \delta = \varphi_{10}. \tag{33}$$

According to Fig. 6 and (31)–(33), it can be seen that the actual phase shift with dead time compensation φ_{1c} is equal to the theoretical phase shift φ_{10}. And the effects of the phase drift phenomenon can be eliminated with dead time compensation.

The operating principle of the proposed method with TDA modeling is shown in Fig. 7. First, the voltage sensors are used to sample the input voltage U_i and output voltage U_o, which are used to calculate the voltage conversion ratio K. The operation mode of the DBSRC is chosen according to K. Second, the outer phase shift θ is the output of the PI controller. Third, the optimal inner phase shift φ_{10} is derived according to Modes I-IV. The expressions of the proposed method with TDA modeling are shown as (30). Then considering the effects of dead time, the compensated optimal inner phase shift φ_{10c} is obtained from (32) in Mode I. Finally, the optimal phase shift ratios are converted into switch signals, which control the MOSFET devices in the DBSRC to achieve power transmission and steady-state performance improvement.

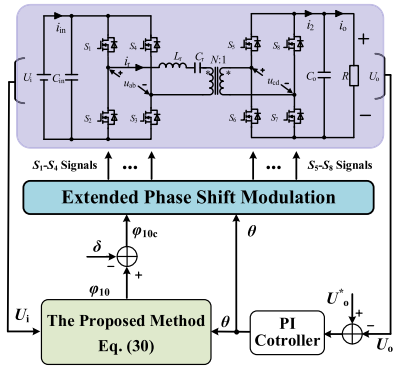

Fig. 7. Block diagram of the proposed method with TDA modeling.

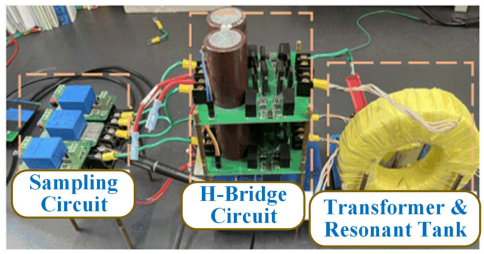

Fig. 8. Photograph of the DBSRC experimental physical prototype.

TABLE II
PARAMETERS OF THE PHYSICAL PROTOTYPE

Parameters	Values
Input voltage	U_i = 180 V
Output voltage	U_o = 144/90 V
Switching frequency	f_s = 100 kHz
Resonant frequency	f_r = 80 kHz
Resonant inductor	L = 40 μH
Resonant capacitor	C = 100 nF
Input/Output capacitor	C_i /C_o = 1120 μF
Load resistance	R = 12.5–45 Ω
Transformer ratio	N : 1=1 : 1

V. EXPERIMENTAL ANALYSIS

A scale-down physical experimental prototype of the DBSRC with TMS320F28335 controller is shown in Fig. 8. The electrical circuit parameters of the physical prototype are shown in Table II. Take $K \leq 1$ as an example, the MCT with FHA modeling and the proposed method with TDA modeling are compared in experimental tests.

A. Comparison Experiments When $K = 0.8$

The experimental parameters are set as $U_i = 180$ V, $U^*_o = 144$ V, $L_r = 40$ μH, $C_r = 100$ nF. When the voltage conversion ratio $K = 0.8$, the operation waveforms of transformer terminal voltages u_{ab}, u_{cd}, and resonant current i_r are shown in Figs. 9 and 10. When $R = 45$ Ω, the operation waveforms in Mode I of the MCT with FHA modeling and the proposed method with TDA modeling are shown in Fig. 9. The efficiency of output power under the MCT with FHA modeling, and the proposed method with TDA modeling are 94.44% and 95.34%.

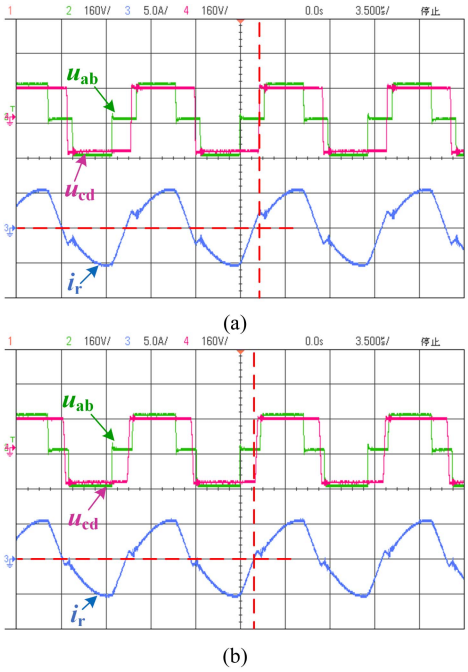

Fig. 9. Experimental waveforms when $K = 0.8$ in mode I. (a) MCT with FHA modeling. (b) Proposed method with TDA modeling.

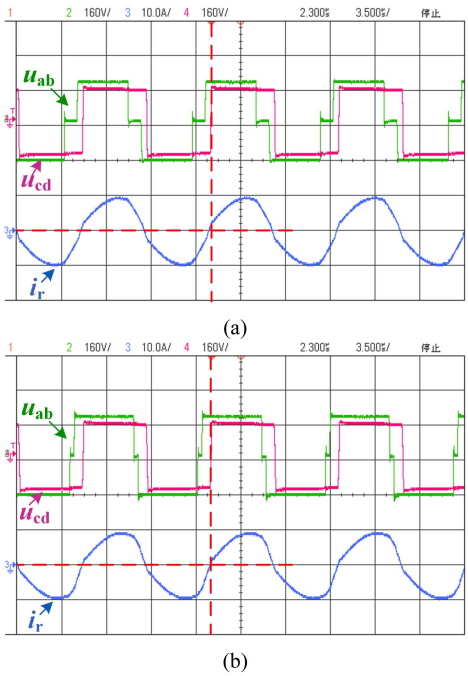

Fig. 10. Experimental waveforms when $K = 0.8$ in mode II. (a) MCT with FHA modeling. (b) Proposed method with TDA modeling.

As shown in Fig. 9(b), the i_r $(\theta) = 0$, and the zero-backflow power optimization have been achieved. However, the i_r $(\theta) > 0$ in Fig. 9(a), which means that compared with the MCT with FHA modeling, the proposed method with TDA modeling can achieve zero-backflow power optimization with high accuracy.

In Mode II, the experimental parameters are set as $U_i = 180$ V, $U^*_o = 144$ V, $L_r = 40$ μH, $C_r = 100$ nF, $R = 22.5$ Ω, and the operation waveforms are shown in Fig. 10. When $K = 0.8$, the efficiency of the DBSRC under the MCT with FHA modeling and the proposed method with TDA modeling are 96.13% and 96.25%, respectively. Besides, as shown in Fig. 10(b), the i_r $(\theta) = 0$, and the zero-backflow power optimization have been achieved. However, i_r $(\theta) > 0$ in Fig. 10(a), which is the same as Mode I.

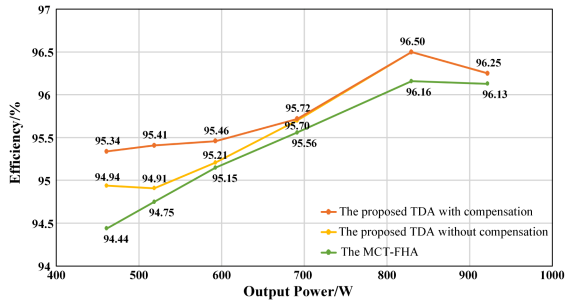

Fig. 11. Efficiency curves of the DBSRC when $K = 0.8$.

Moreover, under different operation conditions, the efficiency curves of the DBSRC under the two control methods are shown in Fig. 11 when $K = 0.8$. As shown in Fig. 11, compared with the MCT with FHA modeling, the proposed method with TDA modeling is of high accuracy and can achieve zero-backflow power optimization. And the efficiency of the DBSRC, especially in light-load, has been improved.

B. Comparison Experiments When $K = 0.5$

To verify the effectiveness of the proposed method with TDA modeling, the experimental parameters are set as $U_i = 180$ V, $U^*_o = 90$ V, $L_r = 40$ μH, and $C_r = 100$ nF. The operation waveforms of the MCT with FHA modeling and the proposed method with TDA modeling are shown in Figs. 12 and 13. In Mode I, when $R = 45$ Ω, the waveforms of the proposed method with TDA modeling are shown in Fig. 12(b), the i_r $(\theta) = 0$, and the zero-backflow power optimization has been achieved. However, the i_r $(\theta) > 0$ in Fig. 12(a), and there is backflow power of the DBSRC under the MCT with FHA modeling. And the efficiency of output power under the MCT with FHA modeling and the proposed method with TDA modeling is 91.00% and 93.00%, respectively.

In Mode II, when $R = 12.5$ Ω, the waveforms of the proposed method with TDA modeling are shown in Fig. 13(b), the i_r $(\theta) = 0$ and the zero-backflow power optimization has been achieved. When $K = 0.5$, the efficiency under the MCT with FHA modeling and the proposed method with TDA modeling are 94.49% and 95.44%, respectively.

Under different operation conditions, the efficiency curves of the DBSRC when $K = 0.5$ are shown in Fig. 14. The zero-backflow power optimization of the DBSRC is remarkable, and the efficiency has been significantly improved. When the voltage conversion ratio K deviates from unity, the zero-backflow power can be greatly reduced due to the proposed method with TDA modeling, which is consistent with the theoretical analysis.

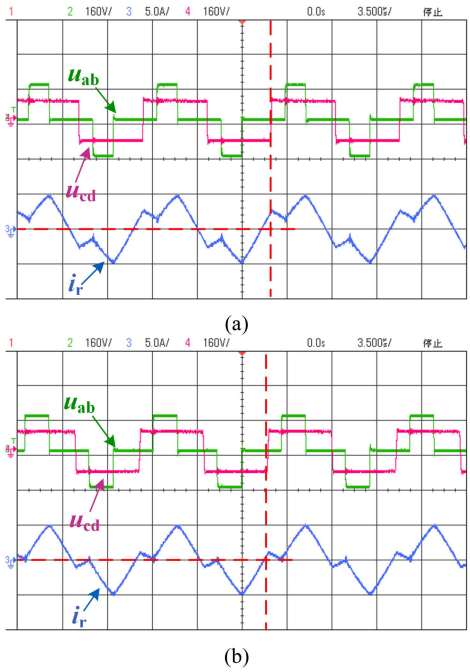

Fig. 12. Experimental waveforms when $K = 0.5$ in mode I. (a) MCT with FHA modeling. (b) Proposed method with TDA modeling.

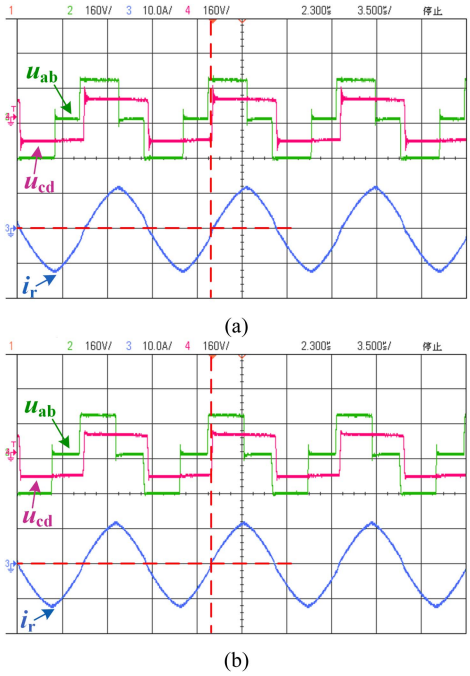

Fig. 13. Experimental waveforms when $K = 0.5$ in mode II. (a) MCT with FHA modeling. (b) Proposed method with TDA modeling.

In summary, the results of comparison experiments verify the effectiveness of the proposed method with TDA modeling, which is the same as the theoretical analysis. When K is far away from unit 1, the performance of the proposed method with TDA modeling is more excellent. The proposed method with TDA modeling can realize zero-backflow power optimization, which

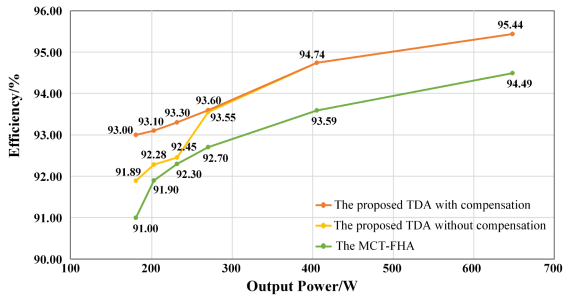

Fig. 14. Efficiency curves of the DBSRC when $K = 0.5$.

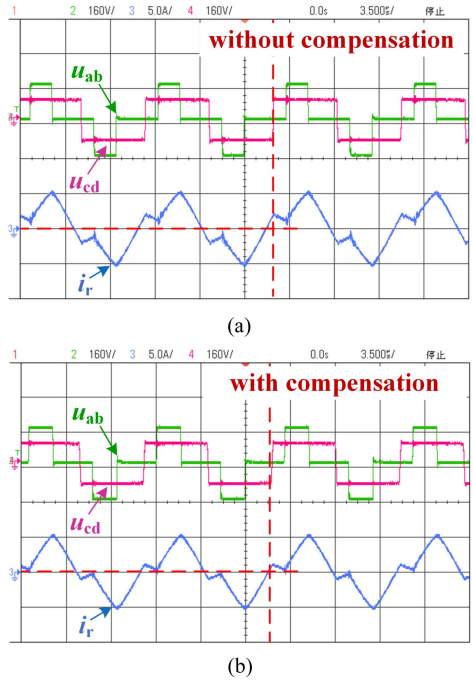

Fig. 15. Experimental waveforms of the proposed method with TDA modeling. (a) Non-dead time compensation. (b) Dead time compensation.

can make up for the error of the FHA model and improve the accuracy of the control algorithm.

C. Dead Time Compensation Experiments

Based on the analysis of the dead time, a compensation method is proposed to eliminate the effects. The dead time compensation experiments of the proposed method with TDA modeling are carried out, and the experimental parameters are set as $U_{\rm i} = 180$ V, $U^*_{\rm o} = 90$ V, $L_{\rm r} = 40$ μH, $C_{\rm r} = 100$ nF, and $R = 40$ Ω. $t_{\rm d} = 300$ ns, the compensation phase shift can be obtained as $\delta = 0.06\pi$.

Only in Mode I, some switches in the DBSRC will lose ZVS, the proposed method can achieve zero-backflow power optimization without dead time compensation in Mode II-IV. The experimental results of the proposed method with TDA modeling without/with dead time compensation are shown in Fig. 15. According to Fig. 15(a), the resonant current $i_{\rm r} > 0$ at the moment of the $u_{\rm cd}$ steps from -90 to 90 V. However, to

realize zero-backflow power optimization, the resonant current should be $i_{\mathrm{r}}=0$ when u_{cd} steps.

Because of the dead time effects, it is unable to achieve zero-backflow power optimization of the DBSRC with the proposed method. As shown in Fig. 15(b), the resonant current is $i_{\mathrm{r}}=0$ at the moment of the u_{cd} steps, and the zero-backflow power is realized because of the accurate proposed control method with dead time compensation. The converter efficiency without compensation is 92.28%, and the efficiency with compensation has been improved to 93.10%. Besides, the efficiency of the proposed method without compensation under different load conditions when $K=0.8$ and $K=0.5$ are shown in Figs. 11 and 14, respectively.

VI. Conclusion

A zero-backflow power optimization under EPS modulation based on the time domain model for the DBSRC is proposed. The transmission power model and resonant tank current model under EPS modulation are analyzed with the TDA method. Then, the backflow power model of the DBSRC based on the TDA with EPS method is given, and the closed-form formulas of zero-backflow power optimization are derived. Besides, the dead time effects are analyzed and the compensation scheme is proposed to improve the accuracy of the control scheme. Finally, the comparison experiments with the MCT with FHA modeling and the proposed method with TDA modeling have been carried out. Comparison results have verified that the proposed method with TDA modeling can achieve zero-backflow power optimization and higher efficiency. The contributions of this article are as follows.

1) Compared to the FHA modeling, accurate models can be obtained by the TDA modeling, which can accurately describe the working characteristics of DBSRCs.
2) Compared with the MCT with FHA modeling, the proposed method with TDA modeling can achieve zero-backflow power optimization and efficiency improvement.
3) The dead time compensation is proposed to eliminate the phase drift phenomenon, which can improve the precision of the proposed method with TDA modeling further.

Appendix I

The initial values of the resonant tank current i_{r} and the resonant capacitor at each stage in Modes I, II, III, and IV are as follows: Unnumbered Eqns. shown at the bottom this page.

$$
\text{Mode I}\begin{cases}
Z_{\mathrm{r}}i_{\mathrm{r}}(0)=-\frac{1}{4}\sec^2(\frac{\pi}{2F})\{U_{\mathrm{i}}[\sin(\frac{\pi}{F})+\sin(\frac{\pi-\varphi_1}{F})-\sin(\frac{\varphi_1}{F})]+2NU_{\mathrm{o}}[\sin(\frac{\theta}{F})-\sin(\frac{\pi-\theta}{F})]\}\\
u_{C_r}(0)=\frac{1}{4}\sec^2(\frac{\pi}{2F})\{U_{\mathrm{i}}[-1+\cos(\frac{\pi-\varphi_1}{F})+\cos(\frac{\varphi_1}{F})-\cos(\frac{\pi}{F})]+2NU_{\mathrm{o}}[1-\cos(\frac{\pi-\theta}{F})-\cos(\frac{\theta}{F})+\cos(\frac{\pi}{F})]\}\\
Z_{\mathrm{r}}i_{\mathrm{r}}(\theta)=\frac{1}{4}\sec^2(\frac{\pi}{2F})\{U_{\mathrm{i}}[\sin(\frac{\theta}{F})-\sin(\frac{\pi+\theta-\varphi_1}{F})-\sin(\frac{\pi-\theta}{F})+\sin(\frac{\varphi_1-\theta}{F})]+2NU_{\mathrm{o}}[\sin(\frac{\pi}{F})]\}\\
u_{C_r}(\theta)=-\frac{1}{4}\sec^2(\frac{\pi}{2F})U_{\mathrm{i}}[\cos(\frac{\pi-\theta}{F})-\cos(\frac{\varphi_1-\theta}{F})-\cos(\frac{\pi+\theta-\varphi_1}{F})+\cos(\frac{\theta}{F})]\\
Z_{\mathrm{r}}i_{\mathrm{r}}(\varphi_1)=-\frac{1}{4}\sec^2(\frac{\pi}{2F})\{U_{\mathrm{i}}[-\sin(\frac{\theta}{F})+\sin(\frac{\pi-\varphi_1}{F})+\sin(\frac{\pi}{F})]+2NU_{\mathrm{o}}[\sin(\frac{\pi-\varphi_1+\theta}{F})-\sin(\frac{\varphi_1-\theta}{F})]\}\\
u_{C_r}(\varphi_1)=-\frac{1}{4}\sec^2(\frac{\pi}{2F})\{U_{\mathrm{i}}[-1+\cos(\frac{\pi-\varphi_1}{F})+\cos(\frac{\varphi_1}{F})-\cos(\frac{\pi}{F})]+2NU_{\mathrm{o}}\\
\quad[1-\cos(\frac{\pi+\theta-\varphi_1}{F})-\cos(\frac{\varphi_1-\theta}{F})+\cos(\frac{\pi}{F})]\}
\end{cases}
$$

$$
\text{Mode II}\begin{cases}
Z_{\mathrm{r}}i_{\mathrm{r}}(0)=-\frac{1}{4}\sec^2(\frac{\pi}{2F})\{U_{\mathrm{i}}[\sin(\frac{\pi}{F})+\sin(\frac{\pi-\varphi_1}{F})-\sin(\frac{\varphi_1}{F})]+2NU_{\mathrm{o}}[\sin(\frac{\theta}{F})-\sin(\frac{\pi-\theta}{F})]\}\\
u_{C_r}(0)=\frac{1}{4}\sec^2(\frac{\pi}{2F})\{U_{\mathrm{i}}[-1+\cos(\frac{\pi-\varphi_1}{F})+\cos(\frac{\varphi_1}{F})-\cos(\frac{\pi}{F})]+2NU_{\mathrm{o}}[1-\cos(\frac{\pi-\theta}{F})-\cos(\frac{\theta}{F})+\cos(\frac{\pi}{F})]\}\\
Z_{\mathrm{r}}i_{\mathrm{r}}(\varphi_1)=-\frac{1}{4}\sec^2(\frac{\pi}{2F})\{U_{\mathrm{i1}}[\sin(\frac{\pi}{F})+\sin(\frac{\pi-\varphi_1}{F})-\sin(\frac{\varphi_1}{F})]+2NU_{\mathrm{o}}[\sin(\frac{\theta-\varphi_1}{F})-\sin(\frac{\pi-\theta+\varphi_1}{F})]\}\\
u_{C_r}(\varphi_1)=\frac{1}{4}\sec^2(\frac{\pi}{2F})\{U_{\mathrm{i}}[1-\cos(\frac{\pi-\varphi_1}{F})-\cos(\frac{\varphi_1}{F})+\cos(\frac{\pi}{F})]+2NU_{\mathrm{o}}\\
\quad[1-\cos(\frac{\pi-\theta+\varphi_1}{F})-\cos(\frac{\theta-\varphi_1}{F})+\cos(\frac{\pi}{F})]\}\\
Z_{\mathrm{r}}i_{\mathrm{r}}(\theta)=-\frac{1}{4}\sec^2(\frac{\pi}{2F})\{U_{\mathrm{i}}[\sin(\frac{\pi-\theta}{F})+\sin(\frac{\pi-\theta+\varphi_1}{F})-\sin(\frac{\theta-\varphi_1}{F})-\sin(\frac{\theta}{F})]-2NU_{\mathrm{o}}\sin(\frac{\pi}{F})\}\\
u_{C_r}(\theta)=-\frac{1}{4}\sec^2(\frac{\pi}{2F})U_{\mathrm{i}}[\cos(\frac{\theta-\varphi_1}{F})+\cos(\frac{\theta}{F})+\cos(\frac{\pi-\theta+\varphi_1}{F})+\cos(\frac{\pi-\theta}{F})-2-2\cos(\frac{\pi}{F})]
\end{cases}
$$

$$
\text{Mode III}\begin{cases}
Z_{\mathrm{r}}i_{\mathrm{r}}(0)=-\frac{1}{4}\sec^2(\frac{\pi}{2F})\{2U_{\mathrm{i}}\sin(\frac{\pi}{F})+NU_{\mathrm{o}}[\sin(\frac{\theta}{F})+\sin(\frac{\varphi_2-\theta}{F})-\sin(\frac{\pi-\theta}{F})-\sin(\frac{\pi-\varphi_2+\theta}{F})]\}\\
u_{C_r}(0)=\frac{1}{4}\sec^2(\frac{\pi}{2F})NU_{\mathrm{o}}[\cos(\frac{\pi-\theta}{F})+\cos(\frac{\theta}{F})-\cos(\frac{\varphi_2-\theta}{F})-\cos(\frac{\pi-\varphi_2+\theta}{F})]\\
Z_{\mathrm{r}}i_{\mathrm{r}}(\varphi_2-\theta)=\frac{1}{4}\sec^2(\frac{\pi}{2F})\{2U_{\mathrm{i}}[\sin(\frac{\varphi_2-\theta}{F})-\sin(\frac{\pi-\varphi_2+\theta}{F})]+NU_{\mathrm{o}}[\sin(\frac{\pi}{F})+\sin(\frac{\pi-\varphi_2}{F})-\sin(\frac{\varphi_2}{F})]\}\\
u_{C_r}(\varphi_2-\theta)=\frac{1}{4}\sec^2(\frac{\pi}{2F})\{2U_{\mathrm{i}}[1+\cos(\frac{\pi}{F})-\cos(\frac{\pi-\varphi_2+\theta}{F})-\cos(\frac{\varphi_2-\theta}{F})]+NU_{\mathrm{o}}\\
\quad[\cos(\frac{\varphi_2}{F})+\cos(\frac{\pi-\varphi_2}{F})-1-\cos(\frac{\pi}{F})]\}\\
Z_{\mathrm{r}}i_{\mathrm{r}}(\pi-\theta)=-\frac{1}{4}\sec^2(\frac{\pi}{2F})\{2U_{\mathrm{i}}[\sin(\frac{\theta}{F})-\sin(\frac{\pi-\theta}{F})]+NU_{\mathrm{o}}[\sin(\frac{\pi-\varphi_2}{F})-\sin(\frac{\varphi_2}{F})+\sin(\frac{\pi}{F})]\}\\
u_{C_r}(\pi-\theta)=\frac{1}{4}\sec^2(\frac{\pi}{2F})\{2U_{\mathrm{i}}[1+\cos(\frac{\pi}{F})-\cos(\frac{\theta}{F})-\cos(\frac{\pi-\theta}{F})]+NU_{\mathrm{o}}[-1-\cos(\frac{\pi}{F})+\cos(\frac{\varphi_2}{F})+\cos(\frac{\pi-\varphi_2}{F})]\}
\end{cases}
$$

$$
\text{Mode IV}\begin{cases}
Z_{\mathrm{r}}i_{\mathrm{r}}(0)=-\frac{1}{4}\sec^2(\frac{\pi}{2F})\{2U_{\mathrm{i}}\sin(\frac{\pi}{F})+NU_{\mathrm{o}}[\sin(\frac{\theta}{F})+\sin(\frac{\varphi_2+\theta}{F})-\sin(\frac{\pi-\theta}{F})-\sin(\frac{\pi-\varphi_2-\theta}{F})]\}\\
u_{C_r}(0)=\frac{1}{4}\sec^2(\frac{\pi}{2F})NU_{\mathrm{o}}[2+2\cos(\frac{\pi}{F})-\cos(\frac{\pi-\theta}{F})-\cos(\frac{\theta}{F})-\cos(\frac{\varphi_2+\theta}{F})-\cos(\frac{\pi-\varphi_2-\theta}{F})]\\
Z_{\mathrm{r}}i_{\mathrm{r}}(\theta)=-\frac{1}{4}\sec^2(\frac{\pi}{2F})\{2U_{\mathrm{i}}[\sin(\frac{\pi-\theta}{F})-\sin(\frac{\theta}{F})]+NU_{\mathrm{o}}[\sin(\frac{\varphi_2}{F})-\sin(\frac{\pi-\varphi_2}{F})-\sin(\frac{\pi}{F})]\}\\
u_{C_r}(\theta)=\frac{1}{4}\sec^2(\frac{\pi}{2F})\{2U_{\mathrm{i}}[1+\cos(\frac{\pi}{F})-\cos(\frac{\pi-\theta}{F})-\cos(\frac{\theta}{F})]+NU_{\mathrm{o}}[-\cos(\frac{\varphi_2}{F})-\cos(\frac{\pi-\varphi_2}{F})+1+\cos(\frac{\pi}{F})]\}\\
Z_{\mathrm{r}}i_{\mathrm{r}}(\varphi_2+\theta)=\frac{1}{4}\sec^2(\frac{\pi}{2F})\{2U_{\mathrm{i}}[\sin(\frac{\varphi_2+\theta}{F})-\sin(\frac{\pi-\varphi_2-\theta}{F})]+NU_{\mathrm{o}}[\sin(\frac{\pi-\varphi_2}{F})-\sin(\frac{\varphi_2}{F})+\sin(\frac{\pi}{F})]\}\\
u_{C_r}(\varphi_2+\theta)=-\frac{1}{4}\sec^2(\frac{\pi}{2F})\{2U_{\mathrm{i}}[-1-\cos(\frac{\pi}{F})+\cos(\frac{\varphi_2+\theta}{F})+\cos(\frac{\pi-\varphi_2-\theta}{F})]+NU_{\mathrm{o}}\\
\quad[1+\cos(\frac{\pi}{F})-\cos(\frac{\varphi_2}{F})-\cos(\frac{\pi-\varphi_2}{F})]\}
\end{cases}
$$

REFERENCES

[1] R. W. A. A. De Doncker, D. M. Divan, and M. H. Kheraluwala, "A three phase soft-switched high-power-density DC/DC converter for high power applications," *IEEE Trans. Ind. Appl.*, vol. 27, no. 1, pp. 63–73, Jan./Feb. 1991.

[2] N. Hou and Y. W. Li, "Overview and comparison of modulation and control strategies for non-resonant single-phase dual-active-bridge DC-DC converter," *IEEE Trans. Power Electron.*, vol. 35, no. 3, pp. 3148–3172, Mar. 2020.

[3] W. Zhou and X. Yuan, "Experimental evaluation of SiC MOSFETs in comparison to Si IGBTs in a soft-switching converter," *IEEE Trans. Ind. Appl.*, vol. 56, no. 5, pp. 5108–5118, Sep./Oct. 2020.

[4] R. Maddipudi, N. Kummari, and S. Chattopadhyay, "A secondary-side phase-shifted bidirectional soft-switching DC-DC converter employing step voltage switching for eliminating device voltage overshoot," *IEEE Trans. Power Electron.*, vol. 38, no. 7, pp. 8583–8596, Jul. 2023, doi: 10.1109/TPEL.2023.3263205.

[5] Z. Zhang, Y.-Y. Cai, Y. Zhang, D.-J. Gu, and Y.-F. Liu, "A distributed architecture based on microbank modules with self-reconfiguration control to improve the energy efficiency in the battery energy storage system," *IEEE Trans. Power Electron.*, vol. 31, no. 1, pp. 304–317, Jan. 2016.

[6] H. Wu, K. Sun, Y. Li, and Y. Xing, "Fixed-frequency PWM-controlled bidirectional current-fed soft-switching series-resonant converter for energy storage applications," *IEEE Trans. Ind. Electron.*, vol. 64, no. 8, pp. 6190–6201, Aug. 2017.

[7] N. Hou and Y. Li, "Communication-free power management strategy for the multiple DAB-based energy storage system in islanded DC microgrid," *IEEE Trans. Power Electron.*, vol. 36, no. 4, pp. 4828–4838, Apr. 2021.

[8] X. She, X. Yu, F. Wang, and A. Q. Huang, "Design and demonstration of a 3.6-kV–120-V/10-kVA solid-state transformer for smart grid application," *IEEE Trans. Power Electron.*, vol. 29, no. 8, pp. 3982–3996, Aug. 2014.

[9] W. Song, M. Zhong, S. Luo, and S. Yang, "Model predictive power control for bidirectional series-resonant isolated DC–DC converters with fast dynamic response in locomotive traction system," *IEEE Trans. Transp. Electrific.*, vol. 6, no. 3, pp. 1326–1337, Sep. 2020.

[10] N. H. Baars, J. Everts, H. Huisman, J. L. Duarte, and E. A. Lomonova, "A 80-kW isolated DC–DC converter for railway applications," *IEEE Trans. Power Electron.*, vol. 30, no. 12, pp. 6639–6647, Dec. 2015.

[11] S. Inoue and H. Akagi, "A bidirectional DC-DC converter for an energy storage system with galvanic isolation," *IEEE Trans. Power Electron.*, vol. 22, no. 6, pp. 2299–2306, Nov. 2007.

[12] A. Emadi, S. S.Williamson, and A. Khaligh, "Power electronics intensive solutions for advanced electric, hybrid electric, and fuel cell vehicular power systems," *IEEE Trans. Power Electron.*, vol. 21, no. 3, pp. 567–577, May 2006.

[13] S. Bhawal, H. Patel, K. Hatua, K. Vasudevan, and S. Bhattacharya, "Solid state transformer based on naturally cell balanced series resonant converter with cascaded H-bridge cells switched at grid frequency," *IEEE Trans. Power Electron.*, vol. 38, no. 7, pp. 8208–8222, Jul. 2023, doi: 10.1109/TPEL.2023.3263754.

[14] J. Shen, J. Zhang, X. Huang, Q. Lin, and Y. Fang, "Active thermal management method for output-parallel DAB DC-DC converters under parameter mismatches and asymmetrical modulation," *IEEE Trans. Power Electron.*, vol. 38, no. 7, pp. 8237–8248, Jul. 2023, doi: 10.1109/TPEL.2023.3266287.

[15] X. Li and A. K. S. Bhat, "Analysis and design of high-frequency isolated dual-bridge series resonant DC/DC converter," *IEEE Trans. Power Electron.*, vol. 25, no. 4, pp. 850–862, Apr. 2010.

[16] X. Liu et al., "Novel dual-phase-shift control with bidirectional inner phase shifts for a dual-active-bridge converter having low surge current and stable power control," *IEEE Trans. Power Electron.*, vol. 32, no. 5, pp. 4095–4106, May 2017.

[17] J. Tian, F. Wang, F. Zhuo, Y. Wang, H. Wang, and Y. Li, "A zero-backflow-power EPS control scheme with multi objective coupled-relationship optimization in DAB-based converter," *IEEE J. Emerg. Sel. Topics Power Electron.*, vol. 10, no. 4, pp. 4128–4145, Aug. 2022.

[18] Y. Tang et al., "Reinforcement learning based efficiency optimization scheme for the DAB DC–DC converter with triple-phase-shift modulation," *IEEE Trans. Ind. Electron.*, vol. 68, no. 8, pp. 7350–7361, Aug. 2021.

[19] F. C. Schwarz, "An improved method of resonant current pulse modulation for power converters," *IEEE Trans. Ind. Electron. Control Instrum.*, vol. IECI-23, no. 2, pp. 133–141, May 1976.

[20] B. Zhao, Q. Song, W. Liu, and Y. Zhao, "Transient DC bias and current impact effects of high-frequency-isolated bidirectional DC–DC converter in practice," *IEEE Trans. Power Electron.*, vol. 31, no. 4, pp. 3203–3216, Apr. 2016.

[21] L. Corradini, D. Seltzer, D. Bloomquist, R. Zane, D. Maksimović, and B. Jacobson, "Minimum current operation of bidirectional dual-bridge series resonant DC/DC converters," *IEEE Trans. Power Electron.*, vol. 27, no. 7, pp. 3266–3276, Jul. 2012.

[22] S. Hu, X. Li, and A. K. S. Bhat, "Operation of a bidirectional series-resonant converter with minimized tank current and wide ZVS range," *IEEE Trans. Power Electron.*, vol. 34, no. 1, pp. 904–915, Jan. 2019.

[23] M. Yaqoob, K. H. Loo, and Y. M. Lai, "A four-degrees-of-freedom modulation strategy for dual-active-bridge series-resonant converter designed for total loss minimization," *IEEE Trans. Power Electron.*, vol. 34, no. 2, pp. 1065–1081, Feb. 2019.

[24] J. Wu, P. Wen, X. Sun, and X. Yan, "Reactive power optimization control for bidirectional dual-tank resonant DC–DC converters for fuel cells systems," *IEEE Trans. Power Electron.*, vol. 35, no. 9, pp. 9202–9214, Sep. 2020.

[25] D. Mou et al., "Reactive power minimization for modular multi-active-bridge converter with whole operating range," *IEEE Trans. Power Electron.*, vol. 38, no. 7, pp. 8011–8015, Jul. 2023, doi: 10.1109/TPEL.2023.3264748.

[26] G. Chen, X. Li, and S. Zhou, "Unified boundary control with phase shift compensation for dual bridge series resonant DC-DC converter," *IEEE Access*, vol. 8, pp. 131137–131149, 2020.

[27] V. Sidorov, A. Chub, D. Vinnikov, and A. Bakeer, "An overview and comprehensive comparative evaluation of constant-frequency voltage buck control methods for series resonant DC–DC converters," *IEEE Open J. Ind. Electron. Soc.*, vol. 2, pp. 65–79, 2021.

[28] B. Zhao, Q. Song, W. Liu, G. Liu, and Y. Zhao, "Universal high-frequency-link characterization and practical fundamental-optimal strategy for dual-active-bridge DC-DC converter under PWM plus phase-shift control," *IEEE Trans. Power Electron.*, vol. 30, no. 12, pp. 6488–6494, Dec. 2015.

[29] S. Wang, Z. Zheng, and Y. Li, "Optimal design methodology of bidirectional dual active bridge series resonant DC/DC converter," in *Proc. IEEE 13th Int. Conf. Power Electron. Drive Syst.*, 2019, pp. 1–5.

[30] R. Oruganti and F. C. Lee, "Resonant power processors, Part I–State plane analysis," *IEEE Trans. Ind. Appl.*, vol. IA-21, no. 6, pp. 1453–1460, Nov. 1985.

[31] S. Wang, Z. Zheng, C. Li, L. Xu, K. Wang, and Y. Li, "Accurate frequency domain analysis and hybrid control method for isolated dual active bridge series resonant DC/DC converters," *Inst. Eng. Technol. Power Electron.*, vol. 12, no. 11, pp. 2932–2941, 2019.

[32] B. Yang, Q. X. Ge, L. Zhao, Z. D. Zhou, and Y. H. Li, "A Small signal model of dual bridge series resonant DC/DC converter for power electronic traction transformer," in *Proc. IEEE Energy Convers. Congr. Expo.*, 2019, pp. 1370–1374.

[33] D. Seltzer, L. Corradini, D. Bloomquist, R. Zane, and D. Maksimović, "Small signal phasor modelling of dual active bridge series resonant DC/DC converters with multi-angle phase shift modulation," in *Proc. IEEE Energy Convers. Congr. Expo.*, 2011, pp. 2757–2764.

[34] E. X. Yang, F. C. Lee, and M. M. Jovanovic, "Small-signal modelling of series and parallel resonant converters," in *Proc. 7th Annu. Appl. Power Electron. Conf. Expo.*, 1992, pp. 785–792.

[35] W. Han and L. Corradini, "Wide-range ZVS control technique for bidirectional dual-bridge series-resonant DC–DC converters," *IEEE Trans. Power Electron.*, vol. 34, no. 10, pp. 10256–10269, Oct. 2019.

[36] S. Yin, Y. Deng, W. Song, J. Chen, and X. Feng, "Global optical control method of dual-bridge series resonant DC/DC converters based on EPS control," *Proc. Chin. Soc. Elect. Eng.*, to be published, doi: 10.13334/j.0258-8013.pcsee.201704.

Yaru Deng (Student Member, IEEE) was born in Yuexi, Sichuan, China, in 1996. She received the B.S. degree in electrical engineering, in 2019, from the Southwest Jiaotong University, Chengdu, where she is currently working toward the Ph.D. degree in electrical engineering.

Her current research interests include optimization control methods of power electronic transformers and dc distribution systems.

Wensheng Song (Senior Member, IEEE) received the B.S. degree in electronic and information engineering and the Ph.D. degree in electrical engineering from the Southwest Jiaotong University, Chengdu, China, in 2006 and 2011, respectively.

From September 2009 to September 2010, he was a Visiting Scholar with the Department of Electrical Engineering and Computer Science, University of California at Irvine, Irvine, CA, USA. From July 2015 to December 2015, he was a Visiting Scholar with the University of Alberta, Edmonton, AB, Canada. He is currently a Full Professor with the School of Electrical Engineering, Southwest Jiaotong University. His current research interests include power electronics, motor drives, railway traction drive systems, and multilevel converters.

Shuai Yin was born in Changsha, Hunan, China, in 1998. He received the B.S. degree in electrical engineering from the Changsha University of Science & Technology, Changsha, China, in 2020. He is currently working toward the M.S. degree in electrical engineering from the Southwest Jiaotong University, Chengdu, China.

His current research interests include optimization control methods of power electronic transformers and dc distribution systems.

Ming Zhong was born in Chengdu, Sichuan, China, in 1996. He received the B.S. and M.S. degrees in electrical engineering from the Southwest Jiaotong University, Chengdu, China, in 2018 and 2021, respectively.

His current research interests include optimization control methods of power electronic transformers and dc distribution systems.

Jian Chen (Member, IEEE) was born in Hubei Province, China, in 1993. He received the B.S. degree in electrical engineering from the Qinghai University, Xining, Qinghai Province, China, in 2016, and the Ph.D. degree in electrical engineering from the Chongqing University, Chongqing, China, in 2021.

He is currently an Assistant Professor with the School of Electrical Engineering, Southwest Jiaotong University, Chengdu, China. His current research interests include wide bandgap device characteristics and models, active gate drivers, and power electronic integration.

Xiaoyun Feng received the B.S., M.S., and Ph.D. degrees in electrical engineering from the Southwest Jiaotong University, Chengdu, China, in 1983, 1988, and 2001, respectively.

From 1998 to 1999, she was a Visiting Scholar with the University of Tokyo, Tokyo, Japan. Since 1983, she has been with the School of Electrical Engineering, Southwest Jiaotong University, where she is currently a Full Professor. Her major research interests include railway optimizing operation, real-time control of train operation, energy-efficient driving, electrical traction converters, and motor drive systems.